



Pergamon

Available online at www.sciencedirect.com

SCIENCE @ DIRECT®



www.actamat-journals.com

Acta Materialia 51 (2003) 1307–1325

Microstructural evolution in adiabatic shear localization in stainless steel

M.A. Meyers^a, Y.B. Xu^b, Q. Xue^a, M.T. Pérez-Prado^a, T.R. McNelley^{c,*}

^a University of California, San Diego, La Jolla, CA 92093-0411, USA

^b Institute of Metals Research, Chinese Academy of Sciences, Shenyang 110016, China

^c Naval Postgraduate School, Monterey, CA, USA

Received 15 February 2001; accepted 30 August 2002

Abstract

Shear bands were generated under prescribed and controlled conditions in an AISI 304L stainless steel (Fe–18%Cr–8%Ni). Hat-shaped specimens were deformed in a Hopkinson bar at strain rates of $ca\ 10^4\ s^{-1}$ and shear strains that could be varied between 1 and 100. Microstructural characterization was performed by electron backscattered diffraction (EBSD) with orientation imaging microscopy (OIM), and transmission electron microscopy (TEM). The shear-band thickness was $ca\ 1\text{--}8\ \mu\text{m}$. This alloy with low-stacking fault energy deforms, at the imposed strain rates (outside of the shear band), by planar dislocations and stacking fault packets, twinning, and occasional martensitic phase transformations at twin-band intersections and regions of high plastic deformation. EBSD reveals gradual lattice rotations of the grains approaching the core of the band. A [110] fiber texture (with the [110] direction perpendicular to both shear direction and shear plane normal) develops both within the shear band and in the adjacent grains. The formation of this texture, under an imposed global simple shear, suggests that rotations take place concurrently with the shearing deformation. This can be explained by compatibility requirements between neighboring deforming regions. EBSD could not reveal the deformation features at large strains because their scale was below the resolution of this technique. TEM reveals a number of features that are interpreted in terms of the mechanisms of deformation and recovery/recrystallization postulated. They include the observation of grains with sizes in the nanocrystalline domain. The microstructural changes are described by an evolutionary model, leading from the initial grain size of $15\ \mu\text{m}$ to the final submicronic (sub) grain size. Calculations are performed on the rotations of grain boundaries by grain-boundary diffusion, which is three orders of magnitude higher than bulk diffusion at the deformation temperatures. They indicate that the microstructural reorganization can take place within the deformation times of a few milliseconds. There is evidence that the unique microstructure is formed by rotational dynamic recrystallization. An amorphous region within the shear band is also observed and it is proposed that it is formed by a solid-state amorphization process; both the heating and cooling times within the band are extremely low and propitiate the retention of non-equilibrium structures. Published by Elsevier Science Ltd on behalf of Acta Materialia Inc.

Keywords: AISI 304L; Stainless steel; Shear bands; Adiabatic deformation; Twinning; Lattice rotation; Amorphization; Recrystallization

1. Introduction

The characterization of post-deformation microstructures is a very important tool in the develop-

* Corresponding author. Tel.: +1-831-656-2589; fax: +1-831-656-2238.

E-mail address: tmcnelley@nps.navy.mil (T.R. McNelley).

ment of our understanding of the thermo-mechanical evolution during shear localization. The question of the correlation of the post-deformation structure with the one evolving during deformation will persist until real-time diagnostics will be developed to characterize the microstructure within the shear bands as it is developing. Nevertheless, significant progress has been made by post-deformation observation and a number of structural alterations have been either suggested or demonstrated. Whereas the older literature classified the shear bands into deformed and transformed (depending on their appearance as observed by optical microscopy), it is now recognized that a broad range of structural alterations is possible: recovery, recrystallization (both dynamic and static), phase transformations, comminution (of brittle materials, amorphization, and crystallization have been discussed. The arsenal of the modern Materials Scientist has recently gained the addition of a powerful new technique, electron backscattering scanning microscopy [1,2]. This method, in combination with transmission electron microscopy (TEM), is helping the elucidation of the deformation/recovery mechanisms. It is impossible to resolve the details of microstructure evolution within shear bands by optical or scanning electron microscopy. Even TEM only reveals the recovered structure, which has undergone the plastic deformation and a complex thermo-mechanical history.

Mataya et al. [3] subjected a stainless steel to high-strain rate deformation and observed a dramatic refinement in the grain size within the shear bands, that they attributed to dynamic recrystallization. Shortly thereafter, detailed observations by TEM were made by Stelly and Dormeval [4], Pak et al. [5], Meyers and Pak [6], and Grebe et al. [7] on shear bands produced in Ti–6%Al–4%V and commercial purity Ti. The electron diffraction patterns inside and outside of the shear band were radically different; outside the band, the characteristic pattern for a single crystalline orientation was clear. Inside the band, a ring-like pattern, produced by many crystallographic orientations, was apparent. The shear band consisted of equiaxed grains with diameters of 0.05–0.2 μm . The dislocation density was relatively low. This remarkable feature

led to the suggestion by Meyers and Pak [6] that the structure was due to dynamic recrystallization. Dynamic recrystallization in Cu was first observed by Andrade et al. [8–10]; in Ti it was confirmed by Meyers et al. [11]; in tantalum, it was observed by Meyers et al. [8], Nesterenko et al. [12,13], and Nemat Nasser et al. [14]; in Al–Li alloys, Chen and Vecchio [15] and Xu et al. [16]; in brass, by Li et al. [17]; in steels, Beatty et al. [18] and Meunier et al. [19] observed equiaxed grains even smaller (0.01–0.05 μm). The shiny, ‘transformed’ appearance reported by many investigators in shear bands in steels may be the result of a fine recrystallized structure with an associated dissolution of carbides, resulting in an increased resistance to etching. These features were in the past mistakenly identified as phase transformation products [20]. The complex thermo-mechanical history of metals in the shear localization regions warrants the questions:

1. Do the observed recrystallized features occur during or after plastic deformation?
2. What is the mechanism of recrystallization?

The goal of this contribution is to address these questions for an AISI 304L SS.

2. Experimental techniques

Shear bands were generated in the AISI 304L SS by two methods as follows.

2.1. The hat-shaped specimen method

The hat-shaped specimen method, using a split Hopkinson bar in the compression mode to generate large shear strains in a small region (*ca.* 200 μm thick). This method, which was developed by Meyer and Manwaring [21], has been successfully used to generate shear localization regions in a number of metals (Ti [11], steels [21], Al alloys [15], Ta [13,14]). It forces shear localization to occur in a narrow region. Thus, even materials that do not localize spontaneously undergo localization in this method. Fig. 1(a) shows a hat-shaped specimen prior to and after being subjected to plastic

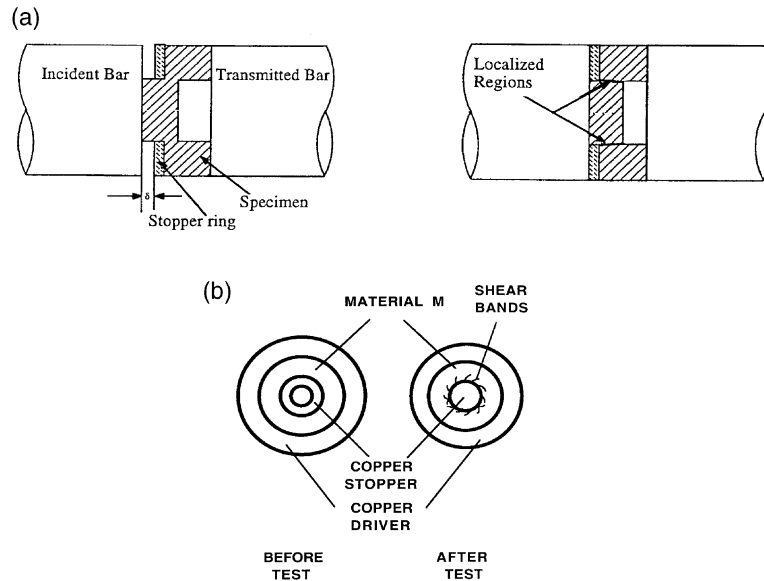


Fig. 1. Schematic of experimental specimens and techniques. (a) Hat-shaped specimen; (b) thick-walled cylinder specimen.

deformation. Prescribed shear strains are obtained by this method, and can be controlled by setting the thickness of the stopper ring. Stopper rings with different thicknesses were used to control the deformation. The displacement δ is shown in Fig. 1(a). Fig. 2 shows the longitudinal section of hat-shaped specimen subjected to a displacement $\delta=1$ mm, yielding a shear strain of $\gamma \approx 100$ if the band width is taken as $10 \mu\text{m}$. Specimens were subjected to displacements providing shear strains of 50, 75, and 100.



Fig. 2. Microstructure of shear band in stainless steel 304L produced in a hat-shaped specimen.

2.2. The explosive collapse of a thick-walled cylinder under controlled conditions

This technique was developed by Nesterenko and Bondar [22] and applied to Ti [23], stainless steel [24], and tantalum [13]. Fig. 1(b) shows the initial configuration of the hollow cylinder in the left and a collapsed cylinder with the shear bands indicated on the right. A regular pattern of spiral shear bands is produced. The inner diameter and the thickness of the inner Cu tube establish the global strain. An explosive charge is placed on the outside and produces, upon detonation, the symmetric implosion of the cylinder. Shear bands initiated at the internal surfaces of the cylinders and propagated outwards along spiral trajectories. The height of the step in the inner surface provides the displacement. The displacement, divided by the thickness of the bands, gives the shear strain. Routinely, shear strains as high as 100 were obtained. Fig. 3 shows the pattern of shear bands observed on the inner surface of the deformed cylinder at an early stage ($\epsilon_{ef}=0.55$); Fig. 3(b) shows the bands at a larger strain ($\epsilon_{ef}=0.92$). It can be seen that the bands form with a characteristic spacing. As the bands grow, their spacing is increased. This occurs

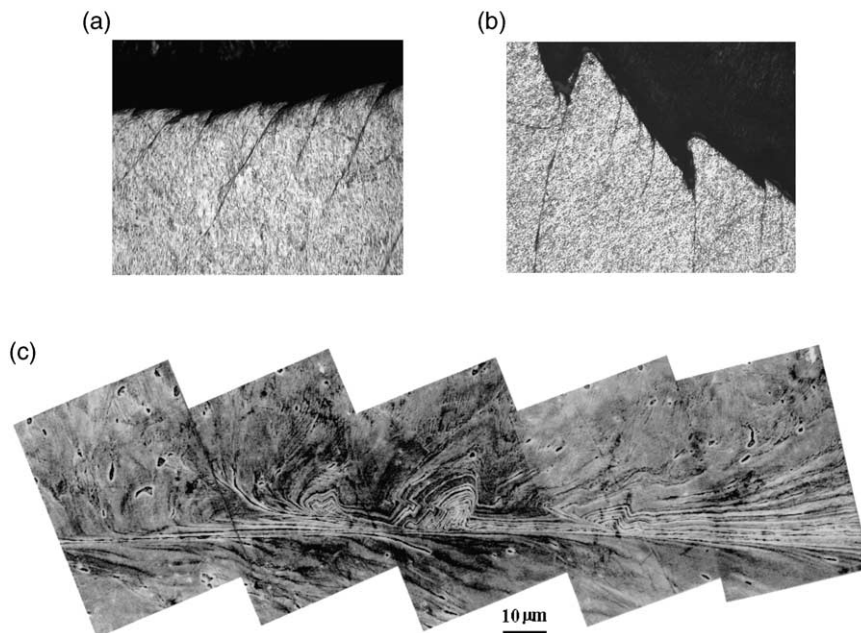


Fig. 3. Shear band pattern at effective strains (a) $\epsilon_{\text{eff}}=0.55$ and (b) $\epsilon_{\text{eff}}=0.92$; (c) shear band in cylindrical collapsed specimen subjected to global $\epsilon_{\text{eff}}=0.92$; note variation in thickness of band and vortex features marked by arrows.

because only a selected fraction of the bands grow. The larger steps exhibited by some of the bands in Fig. 3(b) are indicative of a selection process. Fig. 3(c) shows a SEM montage of a band generated when the cylindrical specimen was subjected to an effective strain of 0.92. Several features deserve mention. First, the thickness of the band is not uniform, but fluctuates between 5 and 50 μm . This is indeed surprising, and indicates that the shear strains would correspondingly fluctuate. Second, the band shows a periodic array of vortex-like features. Vorticity in shear bands has been postulated by Mercier and Molinari [25] and recently observed experimentally by Guduru et al. [26] through temperature measurements and by Nesterenko et al. [27] through recovery experiments in a Nb–Si powder mixture involving the rotation of thin Nb slivers. In Fig. 3, these features appear only on one side of the band and the flow lines show a clear tendency for non-linearity, associated with vorticity. Only a small fraction of shear bands exhibited this behavior. The spacing of the vortices and the fluctuations in thickness are on the scale of the grains (30 μm).

Thus, in the hat-shaped specimen, the bands are forced to form by the highly localized shear strains. In the second case (collapsed thick-walled cylinder), the bands form freely, initiating at the internal surface of the cylinder.

The characterization methods used were TEM and orientation imaging microscopy (OIM) by backscattered electron diffraction (EBSD). Whereas TEM has been employed to characterize shear bands for 20 years (Ti [4,6], Al–Li[9], Ta [12], stainless steel [3], ferritic steels [18,19], brass [17], etc), EBSD is a relatively new characterization technique. The fundamentals of this technique are described in [1,28]. Kikuchi patterns were acquired automatically at steps ranging from 1 to 0.25 μm , and the corresponding orientations were determined utilizing the OIM software provided by TexSem Laboratories, Inc., Provo, UT. This software also allows microstructure mapping by assigning a gray level to each location in the sample (image quality maps). The degree of grayness at a specific location is inversely proportional to the quality of the Kikuchi pattern obtained. For example, grain boundaries or highly deformed

areas are mapped as black regions, since the corresponding Kikuchi patterns are very faint. On the other hand, strain-free regions are depicted as white regions. Due to the high density of Fe, a large amount of electrons from the incident beam are backscattered and, thus, well defined high-intensity Kikuchi patterns can be obtained even when a small beam size is used. Therefore the spatial resolution was increased to *ca.* 0.2 μm . As such, this technique is limited here to determine the orientations of regions of the material that are 0.2 μm or larger. The corresponding orientations were represented by means of direct (111), (011), and (001) pole figures. Boundary character is represented in the form of misorientation distribution histograms.

EBSB was conducted on hat-shaped specimens. Microtexture examination was performed in samples deformed to shear strains (γ) of 50, 75 and 100 (both outside and within the adiabatic shear bands). Sample preparation for EBSB consisted of grinding on successively finer silicon carbide papers followed by mechanical polishing with diamond grit sizes 6 and 1 μm . Final mechanical polishing was performed with a solution of colloidal silica. This solution additionally reacts chemically with the sample surface, aiding to eliminate the superficial deformation layer.

The samples for TEM (both from hat-shaped and thick-walled cylinder specimens) were prepared by sectioning in a high-speed diamond saw, followed by mechanical polishing to a thickness of 100 μm and dimpling to a thickness between 10 and 30 μm . Then, they were either electropolished in a solution of 10% HNO_3 in methanol or ion-beam thinned. Transmission electron microscopy was carried out in JEOL 2000FXII, Philips 420, and JEM 2010 (HREM).

3. Electron backscattered diffraction

Fig. 4 shows the microtexture of the AISI 304L SS in a region far away from the shear band. Fig. 4(a) illustrates direct (100), (110), and (111) pole figures showing a rather weak (almost random) texture. Only a very faint $\langle 111 \rangle$ fiber, with the $\langle 111 \rangle$ direction parallel to the shear direction (SD),

can be construed. The misorientation distribution histogram shown in Fig. 4(b) is formed by the superposition of a Mackenzie-type distribution [29], with a peak around 40° , characteristic of a material with a random texture, and a significant amount (*ca.* 50%) of twin boundaries (misoriented 60°). The peak corresponding to the twin boundaries has been shaded. Fig. 4(c) illustrates OIM map showing the location of the twin boundaries (with the same shade of gray) in the microstructure. For the sake of clarity, only a small portion of the region examined is shown.

Fig. 5 illustrates the microtexture of the grains adjacent to the shear band. The white regions in the center of the OIM map are areas wherein no orientation data could be acquired. This could be due to the presence of a large density of dislocations or of a very fine microstructure, of a smaller scale than the resolution limit of EBSB (*ca.* 0.2 μm). The shear band is located at the center of the OIM map, with the shear direction (SD) parallel to the vertical direction in the map, and the shear plane normal (SPN) parallel to the horizontal direction. It can be seen that grains adjacent to the shear band are elongated, bending slightly towards the SD. Grain subdivision on approaching the shear band can be clearly appreciated. The deformation-induced boundaries [30–32] separating the different subdivided regions lie approximately parallel to the SD. Hansen and coworkers [32–34] have classified deformation-induced boundaries into incidental dislocation boundaries (IDBs) and geometrically necessary boundaries (GNBs). Boundaries resulting from grain subdivision are presumed to be GNBs since, as will be shown later, they have rather large misorientations and they separate regions undergoing independent rotations. Grains subdivide in order to be able to accommodate the imposed shear strain. Lattice rotation has been followed along several paths in the microstructure, depicted in Figs. 5(a–c). The paths in Figs. 5(a, b) run respectively inclined and perpendicular to the shear band, whereas the path depicted in Fig. 5(c) runs parallel to it. The lattice rotation within a (sub) grain (region separated by two deformation induced boundaries) is small (Fig. 5(a)), whereas significant lattice rotations (up to 30°) can be observed when

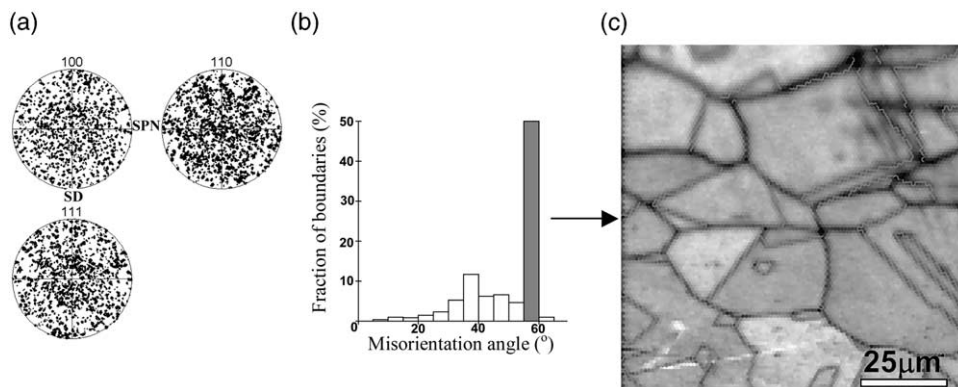


Fig. 4. Microtexture of 304 stainless steel corresponding to a region far away from the shear band. (a) (100), (110), and (111) direct pole figures; the horizontal axis is parallel to the SPN and the vertical axis is parallel to the SD. (b) Misorientation distribution histogram; the peak corresponding to twin boundaries has been shaded in gray. (c) OIM map showing the location of the twin boundaries. Please note that the microtexture data (a) as well as the grain boundary data (b) were measured in a region larger than that shown in (c).

traversing along several (sub) grains (Fig. 5(b)) that initially belonged to the same grain. The misorientation between two adjacent regions resulting from subdivision (i.e. between two (sub) grains) can become rather large, as shown in Fig. 6. There, the point to point and the point to origin cumulative misorientations are plotted versus distance along path B in Fig. 6. Misorientations up to 14° can be observed. Hughes and Hansen [34] observed and modeled grain subdivision into crystallites having large misorientations. They attribute this to the fact that different portions of a grain rotate at different rates and with different rotation axes, resulting in large differences in orientation. The results reported herein are fully consistent with their grain subdivision mechanism. Moreover, it can be observed in Fig. 5(b) that, on approaching the shear band, the lattice rotates until it reaches an end orientation: in this case the $\langle 111 \rangle$ direction becomes aligned with the SD and, simultaneously, a $\{110\}$ plane becomes parallel to the shear plane. This is, presumably, a stable orientation under the shear deformation conditions imposed. Similar lattice rotations were reported in grains adjacent to Ta shear bands [35]. The absence of lattice rotation shown in Fig. 5(a) is consistent with the fact that the lattice has already reached a stable end orientation (again a $\langle 111 \rangle$ direction parallel to the SD and a $\{110\}$ plane parallel to the shear plane). It can also be seen that no boundary is crossed. Other

end orientations found when approaching the shear band along paths perpendicular to the band were, for example: $\{111\}$ plane parallel to shear plane/ $\langle 110 \rangle$ direction aligned with SD, $\sim\{100\}$ plane parallel to shear plane/ $\langle 110 \rangle$ direction aligned with SD. Presumably other end orientations would have been found, if a larger number of grains had been sampled. A common feature of all the end orientations analyzed is the presence of a $\{110\}$ plane perpendicular to both the SD and the SPN.

The observation of several end orientations could be rationalized taking into account that, in addition to accommodating the imposed shear strain, neighboring grains must also deform in a compatible fashion. Fig. 5(c) shows the microtexture along a path parallel to the shear band that comprises several adjacent grains. A fiber texture is formed, in which the fiber axis, close to the $\langle 110 \rangle$ direction, is perpendicular to both the SD and the SPN. Fiber textures also form during tensile deformation of polycrystals due to the need of achieving compatible deformation between neighboring grains [36,37].

Fig. 7 shows the microtexture data corresponding to the core of the shear band. Orientation data could only be acquired in isolated locations (see Fig. 5). The spatial resolution of the EBSD technique is *ca.* $0.2 \mu\text{m}$ and therefore the absence of data in larger regions of the shear band indicates

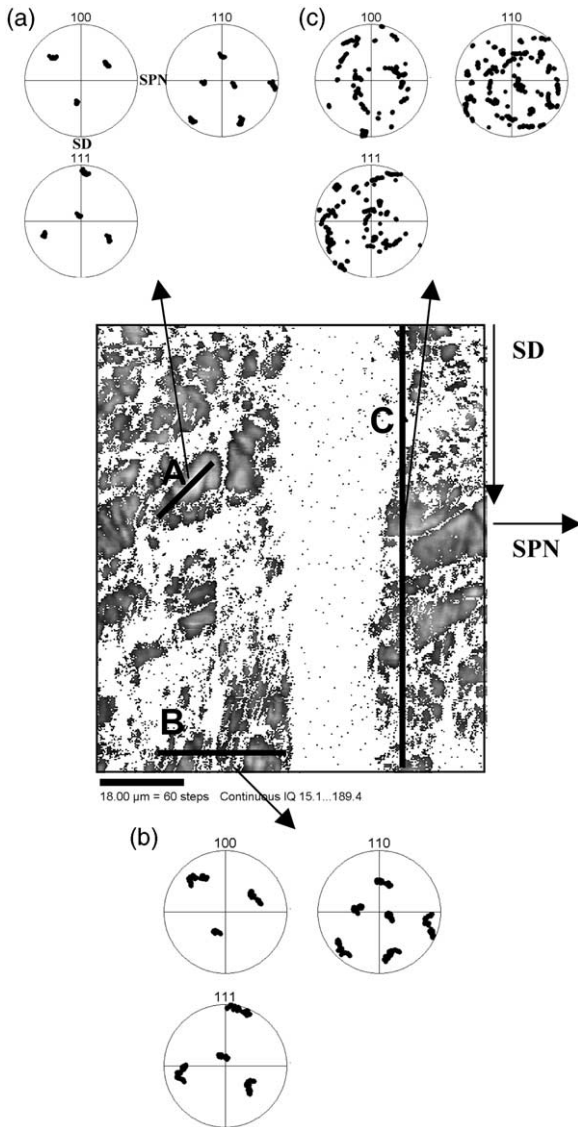


Fig. 5. Microtexture data corresponding to regions adjacent to the shear band. (111), (110), and (100) pole figures showing (a) the lattice rotation within a (sub)grain (path A), (b) the lattice rotation along a subdivided grain (path B), and (c) the microtexture of several adjacent grains (path C). The SD is the vertical and the SPN is the horizontal.

that the scale of the microstructure is smaller than the resolution limit. It is interesting to note that again a fiber texture is formed. The fiber is not perfect since only limited information is available in this region. This is a deformation texture, similar

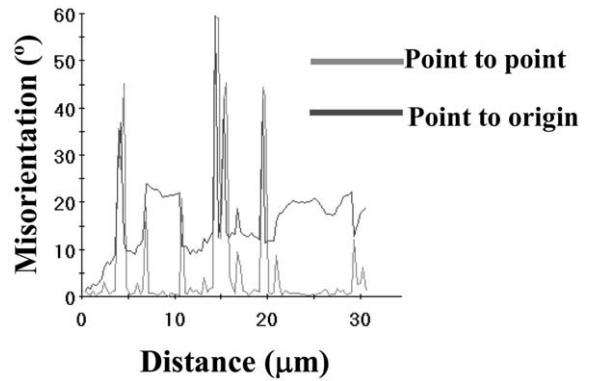


Fig. 6. Point to point and point to origin cumulative misorientation along path B in Fig. 5.

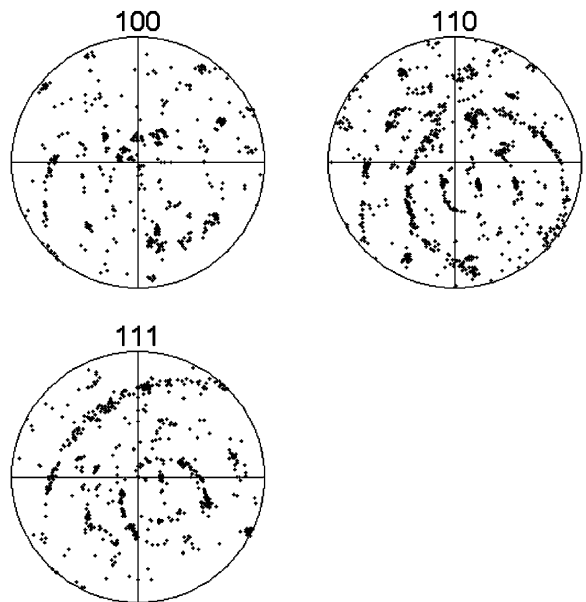


Fig. 7. Microtexture corresponding to regions in the core of the shear band. The SD is the vertical and the SPN is the horizontal.

to that obtained in the grains adjacent to the band. It suggests that grain subdivision continues to take place within the band, with the aim of accommodating the imposed shear strain and maintaining neighboring grain compatibility.

4. Transmission electron microscopy

The AISI 304L SS exhibited, outside of the shear band, the structure characteristic of high-strain rate deformation, which had been systematically identified earlier by Staudhammer et al. [38]. It is characterized by twins and stacking faults, propitiated by the low stacking-fault energy of 304 SS ($\gamma=21 \text{ J/m}^2$ [39]). Fig. 8(a) shows such a structure composed of intersecting twins in a lightly deformed specimen; the foil orientation is close to $[100]$, providing a perpendicular pattern of twins, which are on $\{111\}$. In Fig. 8(b) an incipient shear band is shown. The twins were distorted during severe deformation. These twins have formed prior to the large deformation within the shear bands. They can be formed during the passage of the first shock pulse, which precedes the implosion of the cylinder. Fig. 9(a) shows the twins in greater detail. In addition to the first-order twins, with a spacing of *ca.* $0.1\text{--}0.2 \mu\text{m}$, there are second-order twins, with a much lower spacing. Dark field through the spots indexed in Fig. 9(e) reveals the first-order (Fig. 9(b)) and second-order twins (Fig.9(c)). The matrix channels between the primary twins have a high concentration of dislocations. The second-order twins are imaged in high-resolution microscopy in Fig. 10. The atomic planes (111) are seen and their change in orientation inside the twins are also clear. Two twin sets are seen, with a thickness of *ca.* 20 nm each.

Another very interesting feature observed was the α' martensite which nucleated in the strain bands, particularly at the intersections between twins and bands. Fig. 11 shows an example; the presence of martensite could be confirmed by dark-field image and diffraction analysis; the dark-field image is obtained through the appropriate martensite spot shown in Fig. 11(c). Essentially, these results confirm earlier investigation [38]. These martensite laths nucleate preferentially at twin-band intersections and regions of localized strain. They have been identified by Murr and Rose [40], and Kestenbach and Meyers [41] in connection with shock compression and by Staudhammer et al. [40] in high-strain-rate deformation. The dark-field image shown in Fig. 11(b) comes from the diffraction spot marked by an arrow in Fig. 11(c). Analysis shown in Fig. 11(d) indicates that the $(\bar{1}10)$ planes of the α' martensite are coherent with the $(\bar{1}11)$ planes of the parent austenite, and parallel to each other. The direction, $[\bar{1}10]$ of the α' martensite is parallel to the $[211]$ direction of the austenite, in accordance with the Nishiyama orientation. From this analysis, it is concluded that the $(\bar{1}10)$ of the martensite nucleates along the $\{111\}$ of the austenite. These are the twinning and slip planes; thus, their intersections provide the nucleus, as postulated by Olson and Cohen [42].

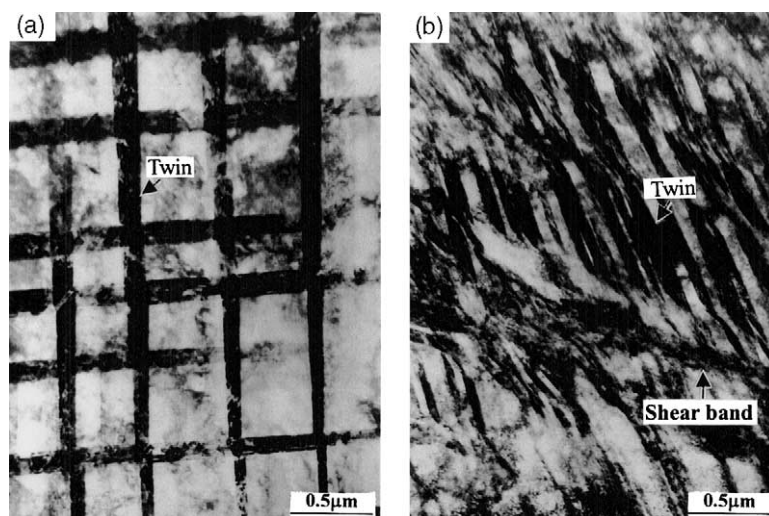


Fig. 8. (a) Deformation twins; (b) intersection between microshear band and deformation twins (distortion in the latter is visible).

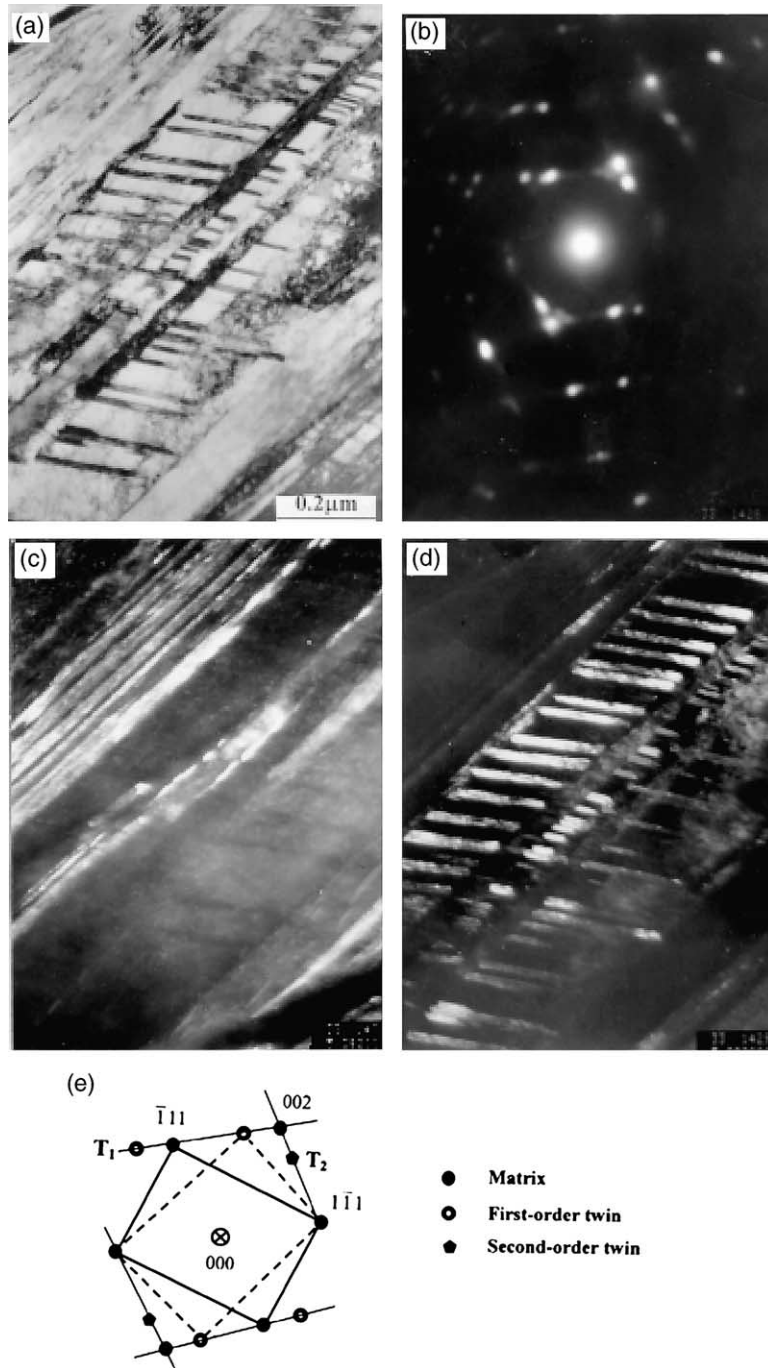


Fig. 9. (a) Bright-field image of the twins; (b) and (c) dark-field images of the first-order twins and second-order twins; (d) corresponding diffraction pattern; (e) indexed the diffraction pattern showing spots for first-order and second-order twins.

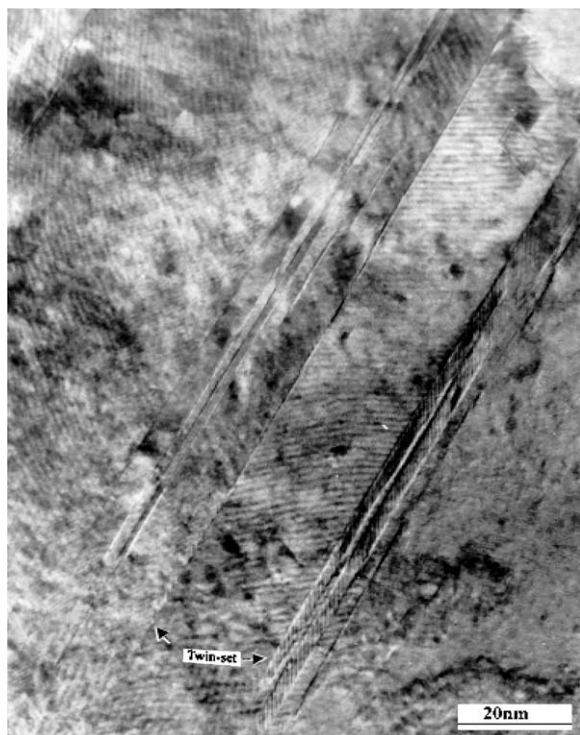


Fig. 10. Multi-order deformation twins imaged by high-resolution TEM.

The microstructure inside of the shear band was radically different from that outside of the band. Two principal domains could be identified:

1. (a) A region composed of nanosized grains in the band. Fig. 12(a) shows this region in bright field. For comparison, the large original grain size of the as-received material ($\sim 30 \mu\text{m}$) with profuse dislocations is shown in Fig. 12(b). The grains within the band (Fig. 12(a)) are smaller, by two orders of magnitude, than the original grains (Fig. 12(b)). Fig. 13 shows a dark field TEM micrograph. The grains are *ca.* 100–200 nm in diameter. These grains have clear boundaries and are equiaxed. This structure is similar to the ones observed in Ti [6,11], Cu [9], Al–Li [15,16], and brass [17]. It has been attributed to a rotational recrystallization mechanism, which was proposed by Meyers et al. [10,11] and later analytically expressed [43,44]. Mataya, Carr, and Krauss [3] were the first to

analyze the fine-grain structure within shear bands in stainless steel; they correctly identified the mechanism for the formation of these grains as dynamic recrystallization. Their plastic deformation was carried out at a much higher temperature, and the grains observed within the shear bands were larger.

2. (b) A glassy region separated from the nanocrystalline region by an interface. Fig. 14 shows the two regions and the interface, with the glassy region at the center and the crystalline one in the periphery. The respective diffraction patterns are also included. Whereas the interface region shows both the ring pattern characteristic of the amorphous phase and spots characteristic of the simultaneous diffraction from many grains, the glassy region shows only the characteristic ring pattern. High-resolution transmission electron microscopy, shown in Fig. 15, confirms the amorphous nature of the material. The absence of imaging from the crystalline planes, in contrast with the crystalline region shown in Fig. 10, is a strong evidence for the lack of crystalline symmetry. This is a surprising finding and is, to the authors' knowledge, the first observation of a crystalline-to-amorphous transition in a shear band. Barbee et al. [45] were able to produce the amorphous phase in 304 SS by sputter depositing it. However, this was only possible for a carbon concentration >5 at%. The clear interface between the amorphous and microcrystalline regions in Fig. 14 and its curved shape suggest a solid-solid transformation. Indeed, since its discovery by Schwarz and Johnson [46], solid-state amorphization has been observed in a variety of systems. This process is especially prevalent in ball milling, where it was first observed by Koch et al. [47]. Sherif El-Eskandarani and Ahmed [48] demonstrated that amorphous $\text{Fe}_{74}\text{Cr}_{18}\text{Ni}_8$ can be produced by ball milling a mixture of elemental Fe, Cr, and Ni powders. Their Fig. 7(d) is very similar to Fig. 14 in this report. Amorphization was found to start after 100 h. The composition $\text{Fe}_{74}\text{Cr}_{18}\text{Ni}_8$ is essentially the same one as AISI 304 SS (Fe–18%Cr–8%Ni). Fecht and Johnson [49,50] give the thermodynamic foundation for solid-state amorphization. In the case of the

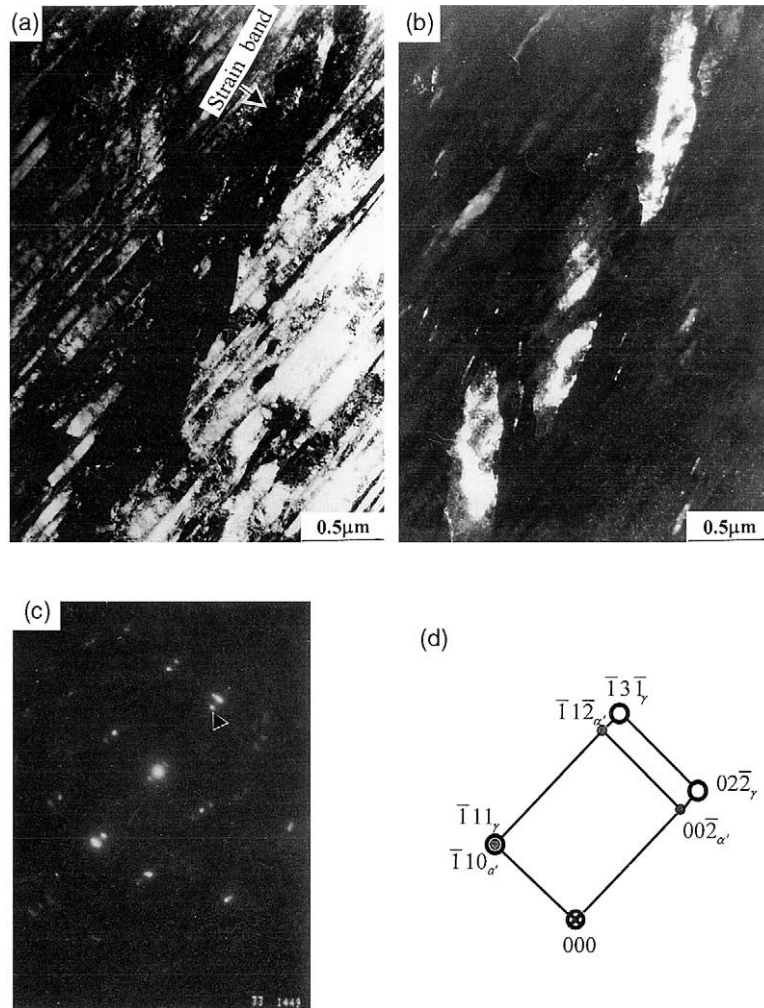


Fig. 11. TEM image showing α' martensite nucleation at the intersection between deformation twins and shear bands; (a) bright field; (b) dark field; (c) diffraction pattern; and (d) indexed diffraction pattern (c).

shear band, there is no reaction and the most feasible explanation is that the material is superheated (beyond its melting point) by plastic deformation. Fig. 16 shows the process in a schematic manner. The enthalpies of solid and liquid phases are plotted as a function of temperature. Melting is a nucleation-and-growth process and the stability limit for the superheated solid (T_i^S) can be up to $1.56\times$ the thermodynamic melting point T_m [50] (for He). In an analogous manner to the glass transition temperature ($T_g < T_m$), an instability temperature for the superheated solid can be defined ($T_i^S > T_m$).

Both T_g and T_i^S correspond to states in which the crystalline and amorphous phases have the same entropy. For Al, $T_i^S = 1.38T_m$; for Nb, $T_i^S = 1.43T_m$; for W, $T_i^S = 1.18T_m$ [49]. Fig. 16 shows the enthalpies of the crystalline and glassy structures in a schematic fashion. At T_m the enthalpy of fusion is ΔH_f . At T_i^S , the enthalpy of melting becomes zero and the crystal could spontaneously convert to the amorphous state (by homogeneous disordering), if the nucleation of the molten phase can be inhibited. Upon cooling, the amorphous phase would be retained since the time to reach T_g would be of

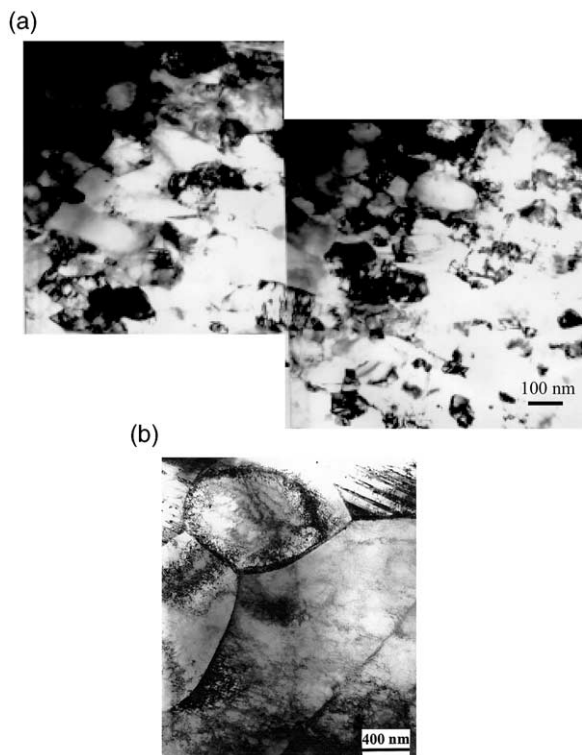


Fig. 12. (a) Microcrystalline structure ($d \sim 100\text{--}200\text{ nm}$) inside bands; (b) large grains outside bands.

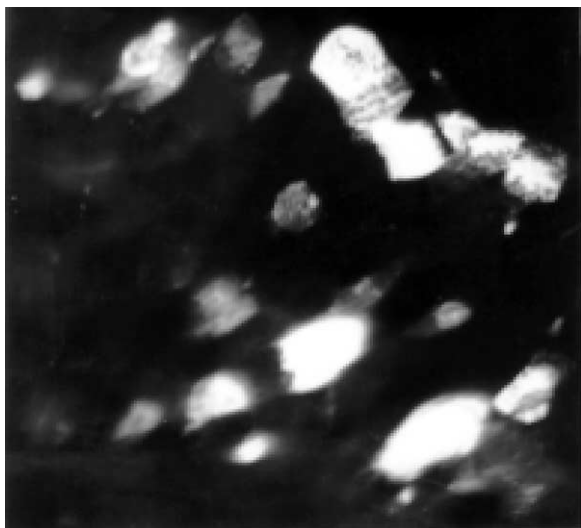


Fig. 13. Dark field of nanocrystalline region.

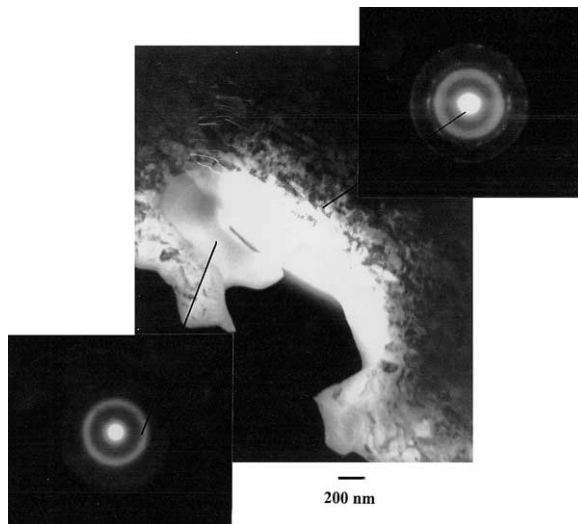


Fig. 14. Nanocrystalline and amorphous regions inside shear band and respective diffraction patterns.

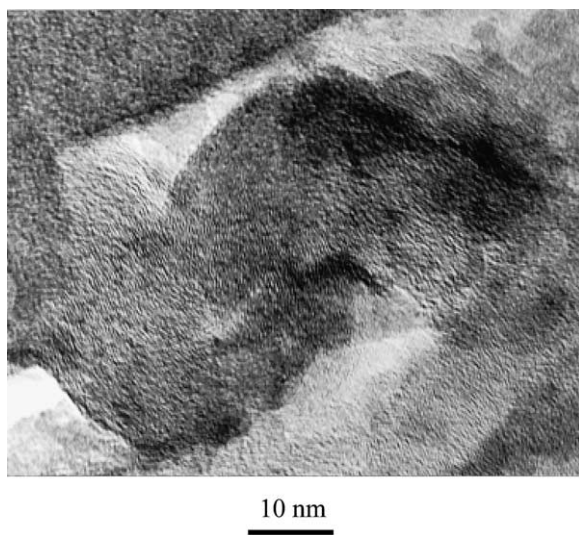


Fig. 15. High-resolution transmission electron micrograph of amorphous region.

a fraction of a millisecond. Thus, the theory proposed by Fecht and Johnson [49] can explain in a successful manner the amorphization observed. This amorphization is enabled by the unique thermomechanical environment extant within the shear band. Both heating and cooling times are on the order of fraction of millise-

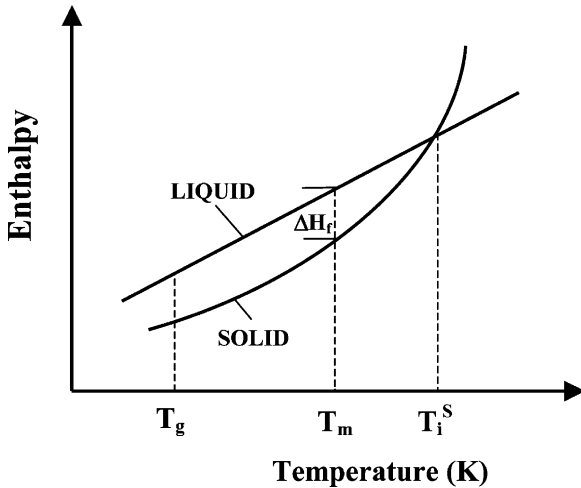


Fig. 16. Schematic representation of enthalpies of liquid and crystalline metal as a function of temperature in the stable and metastable regimes ΔH_f , enthalpy of fusion (adapted from Fecht and Johnson [49]).

conds and nucleation-and growth processes are inhibited. Additional factors that undoubtedly play a role are the high density of point and line defects associated with the large shear strains.

5. Recrystallization

Dynamic recrystallization is usually considered to be a nucleation and growth process, whereby the new grains nucleate either homogeneously or heterogeneously along the original grain boundaries of the deforming material [51]. The definition of the term is broader, and Derby [52] classifies dynamic recrystallization mechanisms into rotational and migrational types. Rotational dynamic recrystallization is well known in geological materials such as quartz, halite, marble, and sodium nitrate; migrational dynamic recrystallization is most common in metals. The current observations (and the earlier ones, on shear bands of Cu, tantalum, brass, steel, and Ti) are suggestive of a rotational dynamic recrystallization mechanism. Meyers and Pak [6] have showed for Ti and Hynes et al. [53] for Cu that the deformation time is lower, by several orders of magnitude, to the time required to create grains of the 0.1 μm size by the

migration of the boundaries. Thus, conventional migrational recrystallization is ruled out. One can envisage the evolution of the microstructure with increasing strain as starting with a homogeneous distribution of dislocations that rearrange themselves into elongated dislocation cells; this stage is often referred to as dynamic recovery. As the misorientation increases, these cells become elongated subgrains. This subgrain subdivision continues as deformation continues. Since different regions of the crystal rotate to different directions, geometrically-necessary boundaries are created [32–34]. These elongated subgrains are a characteristic feature of Cu and Ti subjected to subrecrystallization strains. These elongated structures are seen in many metals subjected to high strains, as reported by Gil Sevillano et al. [54] and Hughes and Hansen [34], among others. This process was modeled by Meyers et al. [43,44] using dislocation energetics.

The relaxation of the broken-down elongated subgrains into an equiaxed microcrystalline structure can occur by minor rotations of the grain boundaries lying along the original elongated boundaries, as shown in Fig. 17. Fig. 17(a) shows the horizontal elongated grains that have already subdivided perpendicular to this plane. This is the most advanced stage of subgrain formation. Minor reorientations of boundary segments are needed to provide a fully recrystallized structure. In Fig. 17(a) if each longitudinal grain boundary segment AB (with length L_1) rotates to A'B' (Fig. 17(b)) by an angle $\theta=30^\circ$, an equiaxed structure will be produced. This is illustrated in Fig. 17(b). It will be shown how this can be accomplished.

It was shown for Cu that these rotations could occur in fractions of millisecond if the length L is sufficiently small [44]. This analysis is reproduced here in a succinct fashion. The flux of atoms along the grain boundary can occur at rates that are orders of magnitude higher than in the bulk. The activation energy for grain-boundary diffusion is approximately one half of that for lattice diffusion, at $T/T_m=0.5$. The ratio between the grain-boundary coefficient of diffusion, D_{OGB} , and lattice coefficient of diffusion, D_{OL} , varies between 10^7 and 10^8 ; these results are reported for FCC metals by Sutton and Balluffi [55] and Shewmon [56].

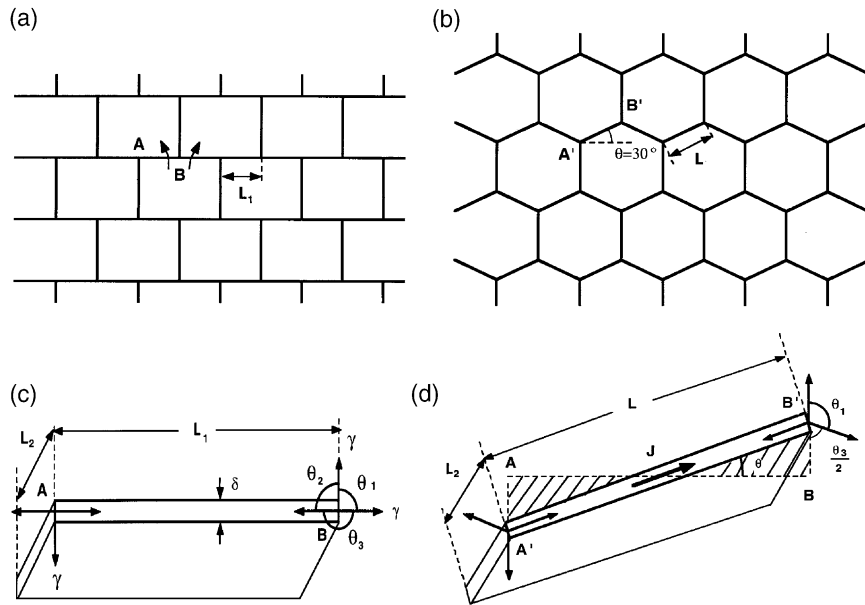


Fig. 17. Rotation of grain boundaries leading to equiaxed configuration: (a) broken down subgrains; (b) rotation of boundaries; (c) a grain boundary AB under effect of interfacial energies; (d) material flux through grain boundary diffusion and rotation of AB to A'B'.

The most general form of Fick’s law, expressed in terms of potential energy gradient acting on a particle, is [56]:

$$\vec{F} = \nabla V \tag{1}$$

where \vec{F} is the force acting on a particle, and ΔV is the gradient of the potential energy field. The mean diffusion velocity \vec{v} is the product of the mobility M by this force ($\vec{v} = M\vec{F}$). The flux along a grain boundary with thickness δ and depth L_2 is equal to (the cross-sectional area is $L_2\delta$):

$$J = L_2\delta C M F = \left(\frac{L_2\delta D C_m}{kT}\right)F, \tag{2}$$

where D is the diffusion coefficient. Fig. 17(c) shows the grain boundary and the forces acting on it. C_m , the concentration of the mobile species, is expressed in terms of mass per unit volume.

The minimization of the interfacial energy is the driving force for the rotation of the boundaries. The force exerted on the grain boundaries is equal to:

$$F = \gamma \left(1 - 2\cos\frac{\theta_3}{2}\right)L_2. \tag{3}$$

This leads to

$$\frac{d\theta}{dt} = \frac{4\cos^2\theta\delta DC_m}{L_1^2\rho kT}\gamma(1 - 2\sin\theta)L_2. \tag{4}$$

Integrating, we arrive at

$$\frac{\tan\theta - \frac{2}{3}\cos\theta}{(1 - 2\sin\theta)} + \frac{4}{3\sqrt{3}}\ln\frac{\tan(\theta/2) - 2 - \sqrt{3}}{\tan(\theta/2) - 2 + \sqrt{3}} + \frac{2}{3} - \frac{4}{3\sqrt{3}}\ln\frac{2 + \sqrt{3}}{2 - \sqrt{3}} = \frac{4\delta D\gamma}{L_1 kT}t. \tag{5}$$

The parameters used in Eq. (5) are: $\gamma=0.625$ J/m² [39]; δ (grain-boundary thickness)=0.5 nm [58]. For AISI 304 SS, $\delta D_{\text{OGB}} = 2 \times 10^{-13}$ m³/s and $D_{\text{OL}} = 3.7 \times 10^{-5}$ m²/s [57]. The activation energies for grain-boundary diffusion and for lattice diffusion for AISI 304 SS are $Q_{\text{GB}} = 167$ kJ/mol and $Q_L = 280$ kJ/mol $Q_L = 280$ kJ/mole [57]. Thus, the grain-boundary diffusion coefficient multiplied

by the grain- boundary thickness is given by Frost and Ashby [57]:

$$\delta D_{GB} = 2 \times 10^{-13} \exp\left(\frac{-167 \times 10^3}{RT}\right).$$

The predictions of Eq. (5) for stainless steel are shown in Fig. 18. In Fig. 18(a), the temperature is varied from 0.40 to 0.55 T_m for a subgrain size of 0.1 μm ; in Fig. 18(b) the subgrain size, L_1 , is varied from 0.1 to 1 μm at $T/T_m=0.5$. The rate of rotation decreases with increasing e and asymptotically approaches 30° as $t \rightarrow \infty$. The collapse time of the thick-walled cylinder is *ca.* 10 μs . The defor-

mation time in the hat-shaped specimen is *ca.* 50 μs . The calculations predict significant rotations of the boundary (within a deformation time of 20 μs) at a temperature of 0.5 T_m , for segment sizes of 0.1 μm (Fig. 18(a)). However, for larger segments the times required are not consistent with the deformation time. Thus, it is concluded that grains with diameters smaller or equal to 0.2 μm can be formed at $T/T_m=0.5$. It should be mentioned that the material is only at a sufficiently high temperature for a fraction of the deformation time. On the other hand, the temperature can easily exceed 0.5 T_m , as will be seen later. Thus, grain- boundary rotation, a necessary step in rotational recrystallization, can take place during plastic deformation. This does not exclude the possibility of reorientation/ accommodation of the grain boundaries during cooling. Thus, it cannot be stated with certainty that the new grains are formed during deformation.

It is also instructive to estimate the temperature inside the shear band as a function of shear strain. This can be done assuming adiabatic conditions, because the thermal diffusion distance is given by

$$x = (\lambda t)^{1/2}, \tag{6}$$

where λ is the thermal diffusivity and t is the time. The thermal diffusivity for iron is *ca.* 0.12 cm^2s^{-1} . The time can be taken as 10–50 μs . Thus, a first estimate for the thermal diffusion distance is 10.7–24.5 μm . The band thickness is 8–20 μm . It is therefore reasonable to assume that most of the heat generated in the plastic deformation process is trapped inside of the shear band (since their thickness is close to the thermal diffusion distance) and that the process is adiabatic.

The following constitutive equation (Zerilli-Annstrong [59]) was used

$$\sigma = C_0 + k_1 d^{-1/2} + C_2 \epsilon^{C_n} \exp(-C_3 T) + C_4 T \ln \dot{\epsilon}, \tag{7}$$

where C_0 , C_2 , C_3 , C_4 , and C_n are experimentally determined parameters. Their values are -76.9 MPa, 2340 MPa, 0.0016 K^{-1} , 0.00008 K^{-1} and 0.36 for stainless steel [60,61]. k_1 is 0.75 $\text{MN m}^{1/2}$. The temperature is obtained by assuming that 90% of deformation work is converted into heat ($\beta=0.9$)

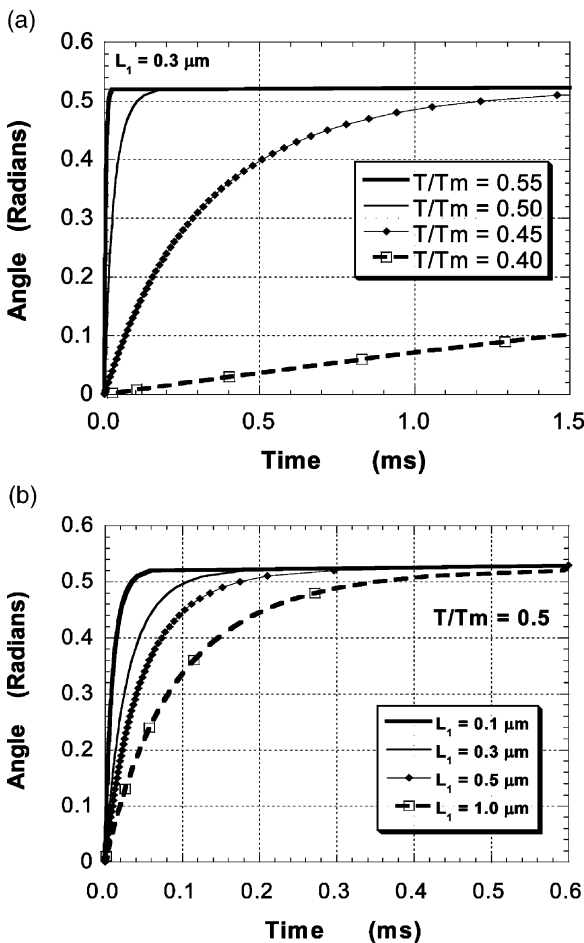


Fig. 18. Angle of rotation of micro-grain boundary AB in 304 stainless steel as a function of time for (a) different temperatures for $L_1=0.1 \mu\text{m}$ and (b) different lengths (0.1, 0.3, 0.5, and 1 μm) at $T/T_m=0.5$.

$$dT = \left(\frac{\beta}{\rho C} \right) \sigma d\epsilon. \quad (8)$$

Integration of Eq. (8), after substituting Eq. (7) into it, leads to T . The parameters for AISI 304L SS were obtained from Kolsky bar experiments and results available in the literature [56]. Fig. 19 shows the temperature as a function of nominal shear strain. It is evident that temperatures close to the melting point can be reached. Hence, the assumption of $T/T_m=0.5$ is justified. This value is reached at a shear strain $\gamma=25$ in Fig. 19.

It should be noted that the shear-band thickness shows considerable variations, as shown in Fig. 3. Thus, the shear strains fluctuate and so should the temperature. This could be responsible for the temperature inhomogeneities measured by Guduru et al. [26]. This can also be responsible for differences in microstructures observed. The propensity for amorphization is highest in a region in which the band thickness is smallest.

The microstructural evolution observed for AISI stainless steel is not expected to be universal. It depends on the temperature evolution within the shear bands and on the cooling rate, among other factors. The propensity to shear localization will also play a role. Indeed, Ta(BCC) and Cu(FCC) are very resistant to shear localization, while steel (BCC) and brass and Al alloys (FCC) are very susceptible. The thickness of the shear localization regions determines the strain, at a fixed displace-

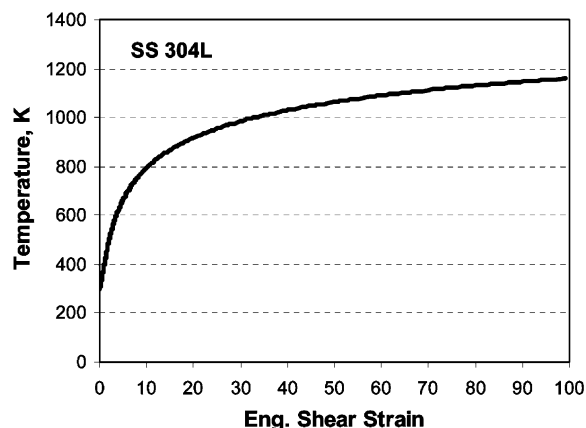


Fig. 19. Temperature as a function of shear strain, assuming adiabaticity, for AISI 304L SS.

ment. Thus, it is expected that different materials will obey different evolution paths. Nevertheless, it is felt that the homologous temperature (T/T_m) within the shear band will dictate the microstructural evolution. In conclusion, it is predicted that the breakup of the microstructure into nanosized grains will occur if global deformation is such that $T/T_m > 0.5$. This has been tentatively verified for Cu [9,10], Ta [13,14], Ti [6,7,11]. The formation of a non-crystalline phase, on the other hand, obeys more complex rules. It is not expected that pure metals will exhibit it, and indeed it has never been observed. The presence of atoms of dissimilar size is one of the metallic glass enablers, and such is the case for the AISI 304 SS.

Question (1) in Section 1 (Do the observed features occur during or after deformation?) cannot be incontrovertibly answered, and it is possible that the process of nanosized grain formation is initiated during deformation and concluded during cooling. The rate of cooling was estimated by Meyers et al. [43,44] for different shear-band thicknesses. The relative times for deformation and cooling vary from specimen top specimen, and, within one specimen, from location to location. It should be noted that recovery/recrystallization processes are temperature dependent and therefore only the higher range of the temperature is effective.

There has been great activity in the field severe plastic deformation (SPD), through which nanocrystalline structures can be obtained for a large number of metals and alloys. The two principal techniques through which this is accomplished are high pressure torsion (HPT) and equal channel angular pressing (ECAP). Valiev and coworkers [62,63], Langdon and coworkers [64,65], and Mukherjee and coworkers [66,67] have applied these methods and determined the nanocrystalline grain size, misorientation between grains, and mechanical properties of metals, alloys, and intermetallics. The microstructures have a considerable resemblance to the ones observed in shear bands. In particular, SPD followed by a low-temperature anneal of Ti showed a grain structure identical to the one observed by Meyers and Pak [6] in Ti. The misorientations between grains have been determined for Ni by OIM by Zhilyaev et al. [65]. The mech-

anisms by which these nanocrystalline structures form are not yet well understood but it seems plausible that the microstructural breakup postulated herein could as well be applicable to SPD. It is indeed interesting to note that the intermetallic compound NiTi yielded an amorphous phase after intense deformation [67]. This is very similar to our current observations. In conclusion, the intense plastic deformation within the shear band is an SPD process. In comparison with HPT and ECAP, the strain rate is much higher. In ECAP, deformation is imparted by successive passes and the temperature rise from deformation is allowed to be equilibrated with the die. In SPD the torsion is continuously applied and the temperature rise is commensurate with the one in a shear band.

6. Conclusions

Shear bands were formed in AISI 304L SS by two different methods: hat-shaped specimen in compression Kolsky-Hopkinson bar and the collapse of a thick-walled cylinder. They were characterized by EBSD and TEM and the evolution of the microstructure is constructed from these post-deformation analyses. EBSD showed grain subdivision in the regions adjacent to the shear band, with angular rotations in the scale of one grain (30 μm) of up to 20°. These rotations are due to the need to accommodate the imposed shear strain as well as to achieve compatible deformation between neighboring grains. As a result, a $\langle 110 \rangle$ fiber texture, with the $\langle 110 \rangle$ axis perpendicular to both the SD and the SPN, forms in the regions adjacent to the band. Inside the shear band, the microstructure breaks down into units smaller than the resolution limit of the EBSD method (0.2 μm), and thus only a very small fraction of these microregions could be sampled. Nevertheless, a $\langle 110 \rangle$ fiber texture, similar to that observed in the regions immediately outside the band, could be observed. This is evidence that the deformation texture is at least partially maintained in the intensely heated region inside the shear band.

Characterization by TEM reveals two regions within the shear bands: (a) a region consisting of grains having sizes of 0.1–0.2 μm with well

defined grain boundaries and a low density of dislocations; (b) a region having a glassy structure. This is the first observation of amorphization within a shear band. Outside of the band, the AISI 304 stainless steel deforms by stacking faults, twinning, and occasional martensitic transformation, as reported earlier [38,40].

These results suggest that the evolution of plastic deformation, coupled with temperature rise, leads from a dislocated/twinned/transformed structure to the breakup into small regions separated by geometrically-necessary boundaries, as defined by Kuhlman-Wilsdorf and Hansen [30]. These regions initiate the process of new grain formation, which requires local grain-boundary rotations. It is shown that these local grain-boundary segments, if having dimensions of 0.1 μm , can rotate by 30° within the deformation time (estimated to be between 10 and 50 μs) and generate an equiaxed microcrystalline structure. The critical requirement is grain-boundary diffusion. A specific mechanism for grain-boundary rotation proposed earlier [44] is applied to AISI 304 SS. This process is called *Rotational Dynamic Recrystallization*, in order to differentiate it from *Migrational Recrystallization* [52]. Nevertheless, one cannot exclude the possibility that the microstructural evolution continues during the cooling stage, after deformation has ceased.

Acknowledgements

Research supported by US Army Research Office MURI Program under Contract DAAH04-96-1-0376, the Department of Energy Grant DEFG0300SF2202, and the Natural Science Foundation of China Grants 50071064 and 19891180-2. Professor V. F. Nesterenko kindly provided us explosively collapsed cylinders of AISI 304 stainless steel. Insightful discussions with Professors K. S. Vecchio and V. F. Nesterenko are gratefully acknowledged.

References

- [1] Adams BL, Wright SI, Kunze K. *Met Trans A* 1993;24A:819.

- [2] Schwarz AJ, Kumar M, Adams BL, editors. Electron backscatter diffraction in materials science. New York: Kluwer/Plenum; 2000.
- [3] Mataya MC, Carr MJ, Krauss. *Met Trans A* 1982;133A:1263.
- [4] Stelly M, Dormeival R. In: Murr LE, Staudhammer KP, Meyers MA, editors. Metallurgical applications of shock-wave and high-strain-rate phenomena. Marcel Dekker; 1986. p. 60-7.
- [5] Pak H-r, Wittman CL, Meyers MA. In: Murr LE, Staudhammer KP, Meyers MA, editors. Metallurgical applications of shock-wave and high-strain-rate phenomena. Marcel Dekker; 1986. p. 60-7.
- [6] Meyers MA, Pak H-r. *Acta Met* 1986;34:2493.
- [7] Grebe A, Pak HR, Meyers MA. *Met Trans A* 1985;16A:761.
- [8] Meyers MA, Meyer LW, Beatty J, Andrade U, Vecchio KS, Chokshi AH. Shock-wave and high-strain-rate phenomena in materials. New York: Marcel Dekker, 1992.
- [9] Andrade UR, Meyers MA, Vecchio KS, Chokshi AH. *Acta Metall Mater* 1994;42:3183.
- [10] Meyers MA, Andrade U, Chokshi AH. *Metall Mat Trans A* 1995;26A:2881.
- [11] Meyers MA, Subhash G, Kad BK, Prasad L. *Mech Mater* 1994;17:175.
- [12] Nesterenko VF, Meyers MA, LaSalvia JC, Bondar MP, Chen Y-J, Lukyanov YL. *Mater Sci Eng* 1997;A229:23.
- [13] Chen Y-J, Meyers MA, Nesterenko VF. *Mater Sci Eng* 1999;A268:70.
- [14] Nemat-Nasser S, Isaacs JB, Liu MQ. *Acta Mater* 1998;46:1307.
- [15] Chen RW, Vecchio KS. *J Physique IV* 1994;4:C8-4591.
- [16] Xu YB, Zhong WL, Chen YJ, Shen LT, Liu Q, Bai YL, Meyers MA. *Mat Sci Eng* 2001;A299:287.
- [17] Li Q, Xu YB, Lai ZH, Shen LT, Bai YL. *Mat Sci Eng* 2000;A276:127.
- [18] Beatty JH, Meyer LW, Meyers MA, Nemat-Nasser S. Shock-wave and high-strain rate phenomena in materials. New York: Marcel Dekker, 1992.
- [19] Meunier Y, Roux R, Moureand J. Shock-wave and high-strain rate phenomena in materials. New York: Marcel Dekker, 1992.
- [20] Rogers HC. *Ann Rev Mat. Sci* 1979;9:283.
- [21] Meyer LW, Manwaring S. In: Metallurgical applications of shock-wave and high-strain-rate phenomena. Marcel Dekker; 1986. p. 657-74.
- [22] Nesterenko VF, Bondar MP. *DYMAT J* 1994;1:243.
- [23] Nesterenko VF, Meyers MA, Wright TW. *Acta Met Mat* 1998;46:327.
- [24] Xue Q, Nesterenko VF, Meyers MA. Shock compression of condensed matter — 1999. *AIP* 2000;2000:431-4.
- [25] Mercier S, Molinari A. *J Mech Phys Sol* 1998;46:1463.
- [26] Guduru PR, Ravichandran G, Rosakis A. SM Report 00-9. California Institute of Technology, 2000.
- [27] Nesterenko VF, Meyers MA, Chen HC, LaSalvia JC. *Appl Phys Lett* 1996;65:3069.
- [28] Randle V. Microtexture determination and its applications. London: The Institute of Metals, 1992.
- [29] MacKenzie JK. *Biometrika* 1958;45:229.
- [30] Kuhlmann-Wilsdorf D, Hansen N. *Scripta Met Mat* 1991;25:1557.
- [31] Bay B, Hansen N, Hughes DA, Kuhlmann-Wilsdorf D. *Acta Metall Mater* 1992;40:205.
- [32] Liu Q, Hansen N. *Scripta Metall Mater* 1995;32:1289.
- [33] Hughes DA, Chrzan DC, Liu Q, Hansen N. *Phys Rev Lett* 1998;81:4664.
- [34] Hughes DA, Hansen N. *Acta Mater* 1997;45:3871.
- [35] Pérez-Prado MT, Hines JA, Vecchio KS. *Acta Mater* 2001;49:2905.
- [36] Pérez-Prado MT, González-Doncel G, Ruano OA, McNelley TR. *Acta Mater* 2001;49:2259.
- [37] Taylor GI. *J Inst Met* 1938;62:307.
- [38] Staudhammer KP, Frantz CE, Hecker SS, Murr LE. In: Shock waves and high-strain-rate phenomena in metals. Marcel Dekker; 1981. p. 91-112.
- [39] Murr LE. In: Interfacial phenomena in metals and alloys. Addison-Wesley; 1975. p. 13-1.
- [40] Murr LE, Rose MF. *Phil Mag* 1968;18:281.
- [41] Kestenbach H-J, Meyers MA. *Met Trans A* 1976;7:1943.
- [42] Olson GB, Cohen M. *Met Trans A* 1976;7A:1897-915.
- [43] Meyers MA, LaSalvia JC, Nesterenko VF, Chen YJ, Kad BK. Recrystallization and related phenomena. In: McNelley TR, editor. *Rex '96*. Monterey; 1997. p. 27-9.
- [44] Meyers MA, Xue Q, Nesterenko VF, LaSalvia JC. *Mat Sci Eng* 2001;A317:204.
- [45] Barbee Jr TJ, Jacobson BE, Keith DL. *Thin Solid Films* 1979;63:143.
- [46] Schwarz RB, Johnson WL. *Phys Rev Lett* 1983;51:415.
- [47] Koch CC, Cavin OB, Mckamey CG, Scarbrough. *Appl Phys Lett* 1983;43:1017.
- [48] El-Eskandarany S, D'Ahmed HA. *Alloys Compounds* 1994;216:213.
- [49] Fecht HJ, Johnson WL. *Nature* 1988;334:50.
- [50] Fecht HJ. *Nature* 1992;356:133.
- [51] Humphreys FJ, Hatherly M. Recrystallization and related annealing phenomena. Oxford: Pergamon, 1995.
- [52] Derby B. *Acta Metall* 1991;39:955.
- [53] Hynes J, Vecchio KS, Ahzi S. *Met Mat Trans A* 1998;29:191.
- [54] Seviliano JG, van Houtte P, Aernoudt E. *Prog Mat Sci* 1981;25:69.
- [55] Sutton AP. In: Interfaces in crystalline materials. Oxford: Clarendon Press; 1995. p. 4-7.
- [56] Shewmon PG. In: Diffusion in solids. 2nd ed. Warrendale, PA: TMS-AIME; 1989. p. 3-1.
- [57] Frost HJ, Ashby MF. In: Deformation mechanism maps. Oxford: Pergamon; 1982. p. 6-2.
- [58] Reed-Hill RE, Abbaschian R. In: Physical metallurgy principles. Boston, MA: PWS Kent; 1992. p. 26-1.
- [59] Zerilli FJ, Armstrong RW. *J Appl Phys* 1990;68:1580.
- [60] Stout MG, Follansbee PS. *Trans ASME J Eng Mat Technol* 1986;198:344.

- [61] Xue Q, Ph. D. Thesis, University of California, San Diego, La Jolla, CA, 2001.
- [62] Valiev R, Chmelik F, Bordeaux F, Kapelsky G, Baudelet B. *Scripta Met* 1996;27:855.
- [63] Mishin OV, Gertsman VY, Valiev RZ, Gottstein G. *Scripta Met* 1996;35:873.
- [64] Furukawa M, Horita Z, Nemoto M, Langdon TG. *J Mater Sci* 2000;36:2835.
- [65] Zhilyaev AP, Kim BK, Nurislamova GV, Baro MD, Szpunar JA, Langdon TG. *Scripta Mat* 2002;575:2002.
- [66] Mishra RS, Stolyarov VV, Echer C, Valiev RZ, Mukherjee AK. *Mat Sci Eng* 2001;A298:44.
- [67] Valiev RZ, Mukherjee AK. *Scripta Met* 2001;44:1747.